

# Experimental Study of the Intrinsic and Extrinsic Transport Properties of Graphite and Multigraphene Samples

J. Barzola-Quiquia, A. Ballestar, S. Dusari and P. Esquinazi  
*Division of Superconductivity and Magnetism, Institute for Experimental Physics II,  
 University of Leipzig  
 Germany*

## 1. Introduction

This chapter<sup>1</sup> deals with the following basic questions, which sometimes surprise or even irritate the reader, namely: Which are the intrinsic properties of the graphene layers inside the graphite structure? Are their transport properties quasi-two dimensional and are they comparable with those of single layer graphene? Which is the coupling between ideal, i.e. defect free, graphene layers inside graphite? Which is the influence of defects and interfaces within the graphene and graphite structure? These basic questions remain in the literature still unanswered to a large extent mainly because the influence on the transport properties of defects and sample or crystal sizes was not systematically taken into account.

A large amount of the published interpretations on the experimental transport data of real graphite samples relied on the assumption that these were intrinsic properties. Let us start with a rather simple example. In the last fifty years scientists flooded the literature with reports on different kinds of electronic measurements on graphite samples, providing evidence for carrier (electron plus hole) densities *per graphene layer* in graphite<sup>2</sup> and at low temperatures  $n_0 > 10^{10} \text{ cm}^{-2}$  as one can read in the standard book from Kelly (1981) or the old publication from McClure (1964), or from more recent work by Grüneis et al. (2008) ( $n_0 \simeq 10^{12} \text{ cm}^{-2}$ ) or Kumar et al. (2010) ( $n_0 \simeq 2.4 \times 10^{11} \text{ cm}^{-2}$ ). But why this concentration is not a constant and does apparently depend on the measured sample? The reader may ask then why at all is the knowledge of the intrinsic carrier concentration  $n_0$  so important?

The carrier concentration is one of those basic parameters needed to estimate several others necessary to get a reliable picture of the electronic band structure and from this to understand all intrinsic (or not) transport properties. For example, two-dimensional (2D) calculations

<sup>1</sup> This work is supported by the DFG under DFG ES 86/16-1. A.B. is supported by the ESF "Nachwuchsforschergruppe" "Funktionale multiskalige Strukturen" and S.D. by the Graduate school of Natural Sciences of the University of Leipzig "BuildMona".

<sup>2</sup> In this chapter and to facilitate a direct comparison between the carrier density of a single graphene layer and that one inside the graphite structure, the carrier density per area will be used. This can be easily obtained multiplying  $n$ , the three dimensional carrier density, by the distance between graphene layers in graphite  $a_0 = 0.335 \text{ nm}$ . This estimate assume that the coupling between graphene layers inside graphite is very weak and that the electron transport is mainly on the two dimensional graphene layers.

assuming a coupling  $\gamma_0$  between nearest in-plane neighbors C-atoms on the graphene plane give a carrier density (per C-atom)  $n(T) = (0.3 \dots 0.4)(k_B T / \gamma_0)^2$  ( $\gamma_0 \simeq 3$  eV and  $T$  is the temperature) (Kelly, 1981). Because all experimental values obtained from bulk graphite samples indicated a finite  $n(T \rightarrow 0) = n_0 > 0$  then the straightforward and "easiest" solution to solve this "disagreement" is to start including more free parameters in the tight-binding electronic band structure calculations.

For example, introducing a new coupling  $\gamma_1$  between C-atoms of type  $\alpha$  in adjacent planes one obtains  $n(T) = a(\gamma_1 / \gamma_0^2)T + b(T / \gamma_0)^2 + c(T^3 / \gamma_0^2 \gamma_1) + \dots$  ( $a, b, c, \dots$  are numerical constants), where the "accepted" value for  $\gamma_1 \sim 0.3$  eV. Also in this case  $n(T \rightarrow 0) \rightarrow 0$ . We stress that neither in single layer graphene nor in graphite such  $T$ -dependence was ever reported<sup>3</sup>, i.e. a large density background  $n_0$  was always measured and assumed as "intrinsic" without taking care of any influence from lattice defects or impurities. To fit experimental data and obtain a finite Fermi energy  $E_F$  – in the simplest case  $E_F \sim \gamma_2$  (Dillon et al., 1977; Kelly, 1981) – up to seven free parameters were and still are introduced, even for carrier density as small as  $n \simeq |-8 \times 10^9| \text{ cm}^{-2}$  ( $E_F \simeq -29$  meV) as obtained recently from magnetotransport data in bulk pyrolytic graphite (Schneider et al., 2009).

Taking into account the exhaustive experience accumulated in gapless or narrow gap semiconductors (Tsidilkovski, 1997) we should actually expect that the measured carrier density  $n_0 \lesssim 10^{12} \text{ cm}^{-2}$  is not intrinsic of the graphite structure but it is influenced by impurities and/or defects in the graphite/graphene lattice. The reader should keep in mind that a carrier density of the order of  $10^8 \text{ cm}^{-2}$  means one carrier in  $1 \mu\text{m}^2$  graphene area, which could be produced actually by having a single vacancy or impurity in the same graphene area, in case one carrier is generated by one of these defects, as experimental (Arndt et al., 2009) and theoretical (Stauber et al., 2007) work suggests. Experimental evidence published recently and partially reviewed in this chapter speaks against an intrinsic origin of – even a part of – the measured  $n_0$  in graphite samples, casting doubts on the relevance of related electronic band structure parameters obtained in the past. On the other hand this new knowledge will help significantly to clarify observed transport phenomena.

In Section 3 of this chapter we describe a method that one can use to obtain the carrier density, the mean free path and the mobility of the carriers inside graphite without free parameters. In that Section we review a systematic study of the transport in small multigraphene<sup>4</sup> samples that reveals room-temperature mobility values ( $\sim 6 \times 10^7 \text{ cm}^2 \text{V}^{-1} \text{s}^{-1}$ ) per graphene layer inside graphite, which overwhelm those reported in literature for single graphene layers, indicating the higher quality of the graphene layers inside ideal graphite. This quality is also reflected by the extremely low room-temperature carrier density ( $\sim 7 \times 10^8 \text{ cm}^{-2}$ ) obtained for good, but certainly not ideal, quality multigraphene samples. These studies indicate that ballistic transport with mean free path in the micrometer range is possible in graphite at room temperature.

In Section 2 we describe the main characteristics of bulk and multigraphene samples, their characterization using transmission electron microscopy (TEM), electron backscattering

<sup>3</sup> It is interesting to note that the carrier concentration obtained in bulk graphite by García et al. (2008), using an original and parameter-free method to determine it and the mean free path, can be fitted up to  $\sim 200$  K by  $n[\text{cm}^{-2}] \simeq n_0 + 10^5 T^2 + 7.5 \times 10^3 T^3$  with  $T$  in [K] and  $n_0 \simeq 2 \times 10^8 \text{ cm}^{-2}$ . The same data, however, can be also well explained by a semiconducting-like exponential function  $\exp(-E_g/2T)$  with an energy gap  $E_g \sim 50$  meV.

<sup>4</sup> We use this word to refer to graphite samples of not more than a few micrometers in length and width and thickness below  $\sim 100$  nm. The reason for this kind of geometrical restriction will become clear in Section 2.

diffraction (EBSD), electronic transport and Raman spectroscopy. We show the correlations between the internal microstructure and sample size – lateral as well as thickness from millimeter size graphite samples to mesoscopic ones, i.e. tens of nanometer thick multigraphene samples – and the temperature ( $T$ ) and magnetic field ( $B$ ) dependence of the longitudinal resistivity  $\rho(T, B)$ . Low energy transmission electron microscopy reveals that the original highly oriented pyrolytic graphite (HOPG) material - from which the multigraphene samples were obtained by exfoliation - is composed of a stack of  $\sim 50$  nm thick and micrometer long crystalline regions separated by interfaces running parallel to the graphene planes (Barzola-Quiquia et al., 2008). We found a qualitative and quantitative change in the behavior of  $\rho(T, B)$  upon thickness of the samples, indicating that their internal microstructure is important. The overall results described in sections 2 and 4 indicate that the metallic-like behavior of  $\rho(T)$  at zero magnetic field measured for bulk graphite samples is not intrinsic of ideal graphite.

The influence of internal interfaces on the transport properties of bulk graphite is described in detail in Section 4 of this chapter. We will show that in specially prepared multigraphene samples the transport properties show clear signs for the existence of granular superconductivity within the graphite interfaces, which existence was firstly reported by Barzola-Quiquia et al. (2008). Based on the results described in Section 4 we argue that the superconducting-insulator or metal-insulator transition (MIT) reported in literature for bulk graphite is not intrinsic of the graphite structure but it is due to the influence of these interfaces.

## 2. Samples characteristics

### 2.1 Sample preparation

In order to systematically study the transport properties of ideal graphite and compare them with those of bulk graphite samples measured in the past, we need to perform measurements in different tens of nanometer thick multigraphene samples of several micrometer square area. The samples presented in this chapter were obtained from a highly oriented pyrolytic graphite (HOPG) bulk sample with a mosaicity (rocking curve width) of  $\sim 0.35^\circ \pm 0.1^\circ$  from Advanced Ceramics company. This material does not only guaranty high crystalline quality but also allows us to easily cleave it and obtain up to several hundreds of micrometers large flakes with thickness from a few to several tens of nanometers. The starting geometry of the bulk graphite material for the preparation of the flakes was  $\sim 1$  mm<sup>2</sup> and  $\sim 20$   $\mu$ m thickness. The selected piece was located between two substrates and carefully pressed and rubbed. As substrate we used p-doped Si with a 150 nm SiN layer on top. The usefulness of the SiN layer on the Si substrate is twofold: firstly the multigraphene flake on it shines with high contrast by illuminating it with white light allowing us to use optical microscopy to select the multigraphene samples.

Immediately after the rubbing process we put the substrate containing the multigraphene films on it in a ultrasonic bath during 2 min using high concentrated acetone. This process cleans and helps to select only the good adhered multigraphene films on the substrate. After this process we used optical microscopy and later scanning electron microscopy (SEM) to select and mark the position of the films. Figure 1 shows four of the investigated samples of different micrometer length and tens of nanometer thickness.

For the preparation of the electrical contacts we used conventional electron beam lithography. The contacts were done by thermal deposition of Pd (99.95%) or Pt/Au (99.5%/99.99%) in high vacuum conditions. We have used Pd or Pt/Au because these elements do not

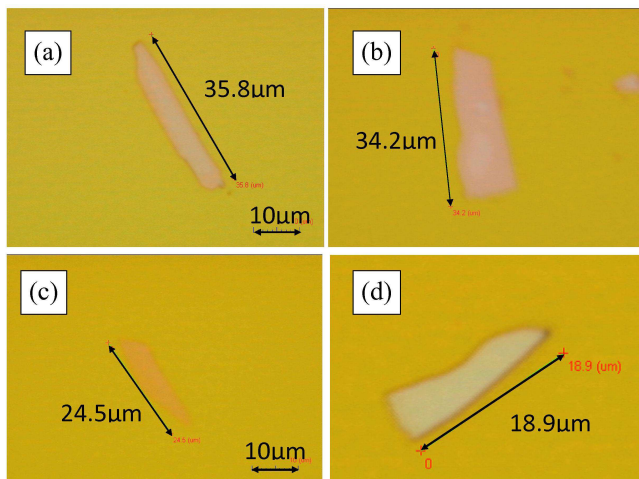


Fig. 1. (a) to (d): Optical microscope pictures of four multigraphene samples prepared as described in the text. The dimensions of the samples can be seen directly at the pictures. The thickness of the samples are: (a) 60 nm, (b) 55 nm, (c) 10 nm, and (d) 85 nm.

show any significant Schottky barrier when used with graphite. This has been checked by  $I - V$  measurements in the temperature range of the measurements used in this work. The advantage of our preparation method lies in the easy way to do (one rubbing process is enough to produce samples, and from the initial flake is possible to produce ten of substrates containing multigraphene samples), it avoids contamination or surface doping avoiding the contact with materials as with the Scotch-tape method. For the transport measurements the substrate with the sample was glued on a chip carrier using GE 7031 varnish. The contacts from the chip carrier to the electrodes on the sample substrate were done using a  $25 \mu\text{m}$  gold wire fixed with silver paste.

## 2.2 Transmission electron microscopy and electron backscattering diffraction

The scanning electron microscope (SEM) pictures, electron beam lithography, lamella preparation and electron backscattering diffraction (EBSD) of the investigated samples were done using a Nova NanoLab 200 dual beam microscope from the FEI company (Eindhoven). A HOPG lamella was prepared for transmission electron microscopy (TEM) using the in-situ lift out method of the microscope. The TEM lamella of HOPG was cut perpendicular to the graphene layers. The electron transmission parallel to the graphene layers provides information on the crystalline regions and their defective parts parallel to the graphene layers. We obtained thin lamellas of around 200 nm thickness,  $\sim 15 \mu\text{m}$  length and  $\sim 5 \mu\text{m}$  width. After final thinning, the sample was fixed on a TEM grid. A solid-state scanning transmission electron microscopy (STEM) detector for high-resolution analysis (included in our microscope) was used. The voltage applied to the electron column was up to 30 kV and the currents used were between 38 pA to 140 pA.

Figure 2 shows the bright (a) and dark field (b) details obtained with the low-voltage STEM at 18 kV and (d) the bright field picture of a different lamella obtained at 30 kV. Figure 2(c) shows a blow out of a detail of (a). The different gray colours indicate crystalline regions with slightly different orientations. The images indicate that the average thickness of the crystalline regions

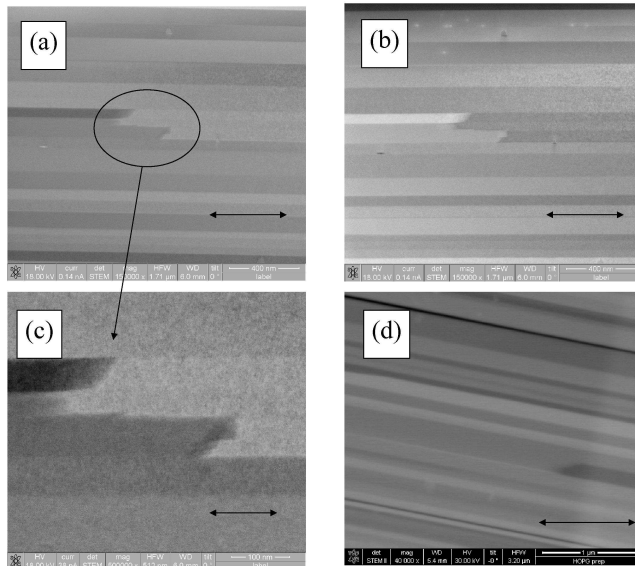


Fig. 2. Transmission Electron Microscopy pictures taken parallel to the graphene layers of two HOPG lamella. The c-axis is perpendicular to the clearly observable stripes of different gray colours, each representing a crystalline region with a slightly different orientation. The arrows in (a) and (b) indicate 400 nm length scale, in (c) 100 nm and in (d) 1  $\mu\text{m}$ . Adapted from Barzola-Quiquia et al. (2008).

is  $60 \pm 30$  nm. One can clearly resolve the interfaces running perpendicular to the c-axis of the layers, parallel to the graphene layers. In Fig. 2(c) we also realize the end of crystalline regions along, normal or with a certain angle respect to the graphene layers direction.

Other experimental technique used to characterize the crystal orientation, defects and grain boundaries is the electron backscattering diffraction (EBSD). The measurements were performed with a commercially available device (Ametek-TSL) included in our microscope. In this setup a cleaved bulk HOPG sample under investigation was illuminated by the SEM beam at an angle of  $70^\circ$  and the diffracted electrons were detected by a fluorescence screen and a digital camera. The included software was used to calculate the orientation of the crystalline regions within the HOPG surface as a function of the electron beam position. Figure 3 shows the grain distribution at the near surface region of a HOPG sample where the in-plane orientation is recognized by the (bluegreen) colour distribution. We recognize in this figure that the typical crystal size (on the (a,b) plane) in our HOPG samples is between a few  $\mu\text{m}$  and  $\sim 20 \mu\text{m}$ . Taking into account the TEM pictures shown in Fig. 2 and the EBSD one in Fig. 3 we conclude that single crystalline regions in a HOPG good quality sample is not more than  $\sim 20 \mu\text{m}$  long and less than  $\sim 60$  nm thick. If the interfaces between the crystalline regions as well as the defects in the crystalline structure in graphite have some influence on the transport properties we then expect to see a change in the behavior of the transport properties between samples of thickness of the order or less than the average thickness of the crystalline regions and of planar size below  $\sim 10 \mu\text{m}$ .

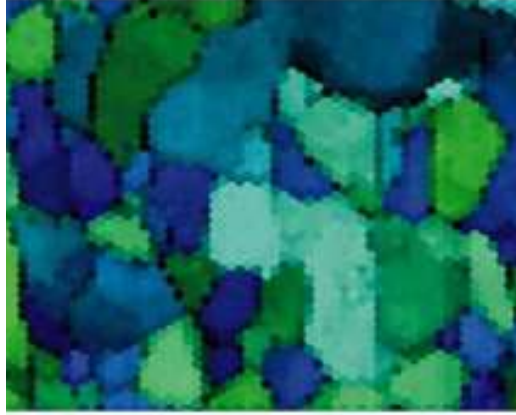


Fig. 3. Electron backscattering diffraction pictures taken from the surface of a HOPG sample. The area scanned is  $\simeq 80 \times 65 \mu\text{m}^2$  and the depth less than 10 nm.

### 2.3 Influence of the internal microstructure on the temperature and magnetic field dependence of the longitudinal resistivity

In order to investigate the intrinsic properties of graphite and taking into account the internal structure of bulk graphite samples, it appears obvious to study tens of nanometers thick graphite samples. Barzola-Quiquia et al. (2008) correlated the internal microstructure and sample size with the temperature and field dependence of the electrical resistivity. Whereas HOPG or graphite samples with thickness larger than  $\sim 50$  nm show a metallic-like behavior in the electrical resistivity vs. temperature, in the case of tens nanometer thick graphite samples, it steadily increases decreasing temperature, see Fig. 4(a).

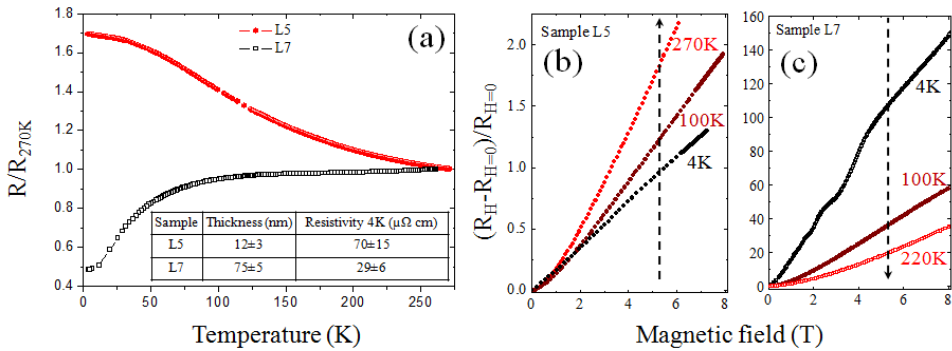


Fig. 4. (a) Normalized resistance versus temperature at zero applied fields for two multigraphene samples, namely: L5 (red dots) and L7 (empty black squares). The values of thickness and resistivity at 4 K are included in the inset table. The magnetoresistance (defined as shown in the y-axis) at three different temperatures are shown for samples L5 (b) and L7 (c). The magnetic field was applied parallel to the c-axis. Adapted from Barzola-Quiquia et al. (2008).



The true temperature dependence of the resistivity in an ideal, defect-free multigraphene sample should be semiconducting-like, as it is expected for an ideal semimetal with zero or small gap. Dusari, Barzola-Quiquia, Esquinazi & García (2011) noted that the temperature dependence of several multigraphene samples shows a semiconducting-like behavior with a saturation or a weak maximum at low temperatures, this last behavior due to the contribution of interfaces, internal as well as with the substrate or at the free sample surface, parallel to the graphene layers, see also Section 4. It becomes now clear that the contribution of the interfaces to the measured conductance of large samples can overwhelm the one coming from the intrinsic graphene layers in thick enough samples. Recently done studies on several graphite samples of different thickness indicate the existence of an intrinsic energy gap of the order of 40 meV in the graphene layers within ideal Bernal graphite (García et al., 2011). We note that experiments on samples with carrier concentration  $\lesssim 10^9 \text{ cm}^{-2}$  are hardly reported in literature. At such low-carrier densities, as it appears to manifest in graphite, electron correlations and possible localization effects should be considered. Electron interactions are large and for a small-enough carrier density, the expected screening will be very weak promoting therefore the existence of an energy gap (Drut & Lähde, 2009).

According to literature the structural quality of graphite samples can be partially resolved by investigating the Raman D-line at  $\sim 1350 \text{ cm}^{-1}$ . However, also the edges of the samples as well as the borderlines between regions of different thicknesses may contribute to the D-band signal. The Raman spectra between 1300 and  $1700 \text{ cm}^{-1}$  have been measured at different positions of several multigraphene samples by Barzola-Quiquia et al. (2008). Those results show that in thin multigraphene samples with similar semiconducting-like behavior in the temperature dependence of the resistivity, different amplitudes of the Raman D-line peak are measured. This indicates that the disorder related to this Raman line does not appear to affect strongly the temperature dependence of the resistivity.

As the absolute value of the electrical resistivity depends also on the measured sample thickness, see Section 2.4, it seems clear to assume that the metallic-like behavior is not intrinsic to ideal graphite but it is due to the influence of the interfaces inside the graphite samples with large enough thickness. Magnetoresistance (MR) results follow the behavior observed in the electrical resistivity. If a metallic behavior is obtained (thicker samples) then the MR decreases with increasing temperature and it shows SdH oscillations, see Fig. 4(c). If the graphite sample shows a semiconducting-like behavior (thinner samples) then the MR is clearly smaller in magnitude as well as it *decreases* decreasing temperature for fields above 1 T, see Fig. 4(b). This figure also shows the absence of the SdH oscillations when the thickness of the graphite sample is small enough.

We note that Kohler's rule does not apply in multigraphene and HOPG samples and one of the reasons might be the contribution of the sample internal structure and interfaces. Defects and interfaces may influence the dimensionality of the transport and might be the origin of localized granular superconductivity. Results presented so far correspond to the situation in which the field is parallel to the c-axis. In the case of having magnetic field applied parallel to the graphene planes nearly no MR is observed. This fact speaks for a huge anisotropy of the metallic or superconducting regions and it suggests that those are within the interfaces found by TEM, see Fig. 2. We note that the field-induced metal-insulator transition (MIT) found in bulk HOPG samples, see Section 4.2, vanishes for samples thinner than 50 nm, which also indicates that certain regions parallel to graphene planes are related to the origin of this MIT (Barzola-Quiquia et al., 2008).

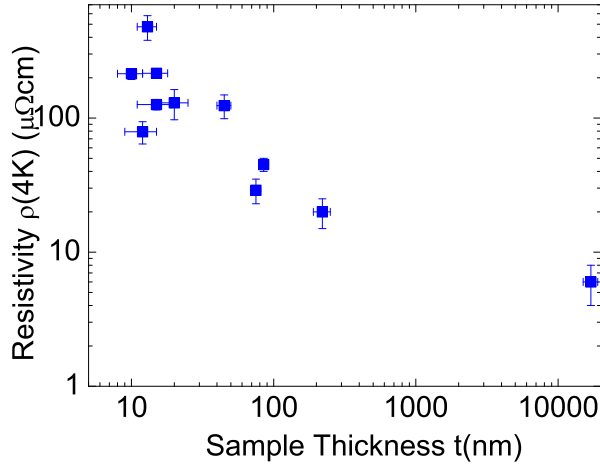


Fig. 5. Resistivity at 4 K vs. sample thickness of different samples obtained from the same HOPG bulk sample.

#### 2.4 Thickness dependence of the resistivity

Figure 5 shows the resistivity at 4 K of different samples vs. their thickness. It is clearly seen that the resistivity decreases increasing the sample thickness. The average change in resistivity between  $\sim 10$  nm to  $17 \mu\text{m}$  thick samples is about two orders of magnitude, far beyond geometrical errors. A possible explanation for the observed behavior is that the larger the thickness the larger the amount of interfaces in the sample, see Fig. 2. As we described in Section 2.3, there is a clear change in the temperature and magnetic field dependence decreasing the sample thickness. It appears unlikely, however, that randomly distributed point-like lattice defects can be the reason for the observed behavior. Also the interpretation provided by Zhang et al. (2005) that the decrease of mobility  $\mu$  (i.e. an increase in the resistivity at constant carrier density) decreasing sample thickness provides an evidence for boundary scattering is surely not the correct explanation for the observed behavior, taking into account the fact that one graphene layer shows finite and large mobility. Note that thin graphite flakes show ballistic transport with huge mobilities, see Section 3. The overall results suggest the existence of a kind of thickness-threshold around  $\sim 50$  nm for multigraphene samples of few micrometers size, obtained from HOPG bulk graphite indicating that the interfaces contribute substantially and in parallel to the graphene layers.

In the past the influence of the internal interfaces in graphite bulk samples was either completely neglected or the scientific community was not aware of their existence. On the other hand it is well known that grain boundaries in various semiconductors can lead to the formation of quasi-two dimensional carrier systems confined in the boundaries. As early examples in literature we refer to the quasi-two dimensional electron gas system that was found at the inversion layers of n-Ge bicrystals (Uchida et al., 1983; Vul & Zavaritzkaya, 1979) or in p-InSb (Herrmann et al., 1984) as well as in  $\text{Hg}_{1-x}\text{Cd}_x\text{Te}$  grain boundaries (Ludwig et al., 1992). It is important to note that in Ge-bicrystals Uchida et al. (1983) found actually the quantum Hall effect (QHE) at  $T \leq 4.2$  K and at magnetic fields above 6 T. The density of carriers at the interface was estimated to be  $\sim 5 \times 10^{12} \text{ cm}^{-2}$ . Therefore, we note that the usually reported carrier concentrations for graphite are not intrinsic of ideal graphite,



as shown by Arndt et al. (2009) and also by Dusari, Barzola-Quiquia, Esquinazi & García (2011). Furthermore, we speculate that the QHE behavior observed in bulk graphite samples (Kempa et al., 2006; Kopelevich et al., 2003) comes from internal interfaces.

### 3. Searching for the intrinsic transport properties of the graphene layers inside graphite

#### 3.1 Background

In this Section we will briefly discuss the background of the ballistic transport and its experimental observation in graphene layers inside the graphite structure. The wave nature of the electrons plays an important role when the sample dimensions are comparable with the wavelength of the electrons. This turns to be possible in graphite samples because the density of carriers is very small, increasing therefore the Fermi wavelength  $\lambda_F$ . On the other hand, as we will see below, a carrier within the graphene layers inside graphite can transit micrometers through the sample without collisions. Therefore the carriers in the graphene layers within an ideal graphite structure have the unusual property of having large  $\lambda_F$  as well as large mean free path  $\ell$ .

The transport phenomenon in the ballistic regime is best described by the Landauer approach. Consider a narrow constriction connected through two wide contact leads across which a voltage is applied. Let the electrochemical potentials of two regions be  $\mu_1$  and  $\mu_2$ . The net current flowing through the device can be taken as  $I = (2e^2/h) \sum T_i (\mu_1 - \mu_2)$  where  $T_i$  is the transmission probability of carriers and the factor 2 comes from the spin degeneracy in each sub-band (Büttiker, 1986; Landauer, 1957; Tsu & Esaki, 1973). The effective conductance through a narrow constriction is given by  $G = I/(\mu_1 - \mu_2) = (2e^2/h) \sum T_i$ . When the constriction dimensions are comparable to  $\lambda_F$  and much shorter than the mean free path  $\ell$ , one can see steps in the conductance when the constriction width is varied. These steps are nearly integer multiples of  $(2e^2)/h$ . Conductance quantization can be also achieved by varying the potential energy. As the constriction width is reduced or the gate voltage is changed in a determined direction, the number of propagating modes at a given energy decreases, i.e. the sub-bands are cut off one by one, and therefore the conductance decreases. A new mode appears in the conductance when the constriction width increases by  $\lambda_F/2$ .

Nowadays, it is feasible to fabricate devices that show ballistic transport. However, it is difficult and time consuming to fabricate these devices because of the required small dimensions when common metals or semiconductors are used. In the past there were some experiments revealing conductance quantization at low temperatures. The first experimental observations of conductance quantization in two dimensional electron gases (2DEG) were reported by van Wees et al. (1988) and Wharam et al. (1988). They studied the point contact conductance in GaAs-AlGaAs heterostructures as a function of a negative gate voltage at low temperatures. The conductance showed clear plateaus at integer multiples of  $2e^2/h$  as the width increases by an amount of  $\lambda_F/2$ . In both cases the authors could show that the transport is completely ballistic and the conductance is determined by the number of occupied sub-bands, independently of the channel length.

#### 3.2 Ballistic transport in graphite

For decades, the transport properties of bulk graphite were interpreted using Boltzmann-Drude approach assuming diffusive ohmic behavior for the conduction electrons (Kelly, 1981). Within this approach one has four temperature-dependent free parameters, namely two mobilities and two carrier densities. The determination of these parameters

using this model implies fitting transport data with at least four free parameters. To obtain accurate values for these parameters it is necessary, however, to go beyond this model. When the mean free path and Fermi wavelength are of the order of sample size, one is not allowed to use the Boltzmann-Drude transport theory to determine the electrical resistance. As discussed before if the size of the system is of the order or smaller than the carrier mean free path, ballistic regime enters in which carriers can move through the system without experiencing any scattering. Usually in metals this takes place in the nanometer range. However, graphite is extraordinary because its mean free path is of the order of microns (Dusari, Barzola-Quiquia, Esquinazi & García, 2011; García et al., 2008).

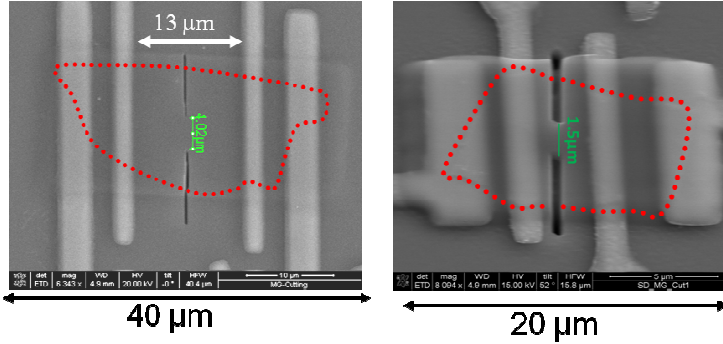


Fig. 6. Scanning electron microscope pictures of the two multigraphene samples, A (left) and B (right) with the Pd electrodes. Sample A has a constriction of  $4\mu\text{m}$  and sample B of  $1.5\mu\text{m}$ . The scale bar in sample A indicates  $10\mu\text{m}$  and in sample B  $5\mu\text{m}$ . The dashed red lines denotes the border of the multigraphene samples.

There is a transparent method to obtain all the main transport parameters from experiments based on constrictions prepared in the graphite or multigraphene samples (García et al., 2008). When the mean free path is larger than the constriction width ( $W$ ), the transport of the carriers shifts from ohmic to ballistic (Sharvin, 1965). By measuring the longitudinal resistance as a function of the constriction width, one can determine the mean free path, carrier density and Fermi wavelength (Dusari, Barzola-Quiquia, Esquinazi & García, 2011; García et al., 2008). Consider the geometry depicted in Fig. 1 of García et al. (2008), or the samples in Fig. 6, for a constriction in a quasi-two dimensional sample. Already Maxwell pointed out that a constricting circular orifice of diameter  $W$  in a thin, nontransparent screen of size  $L_s$  produces a spreading resistance that is equal to the  $\rho(T)/W$  if the ratio  $\ell/W \ll 1$  ( $\rho$  is the resistivity of the material). However, when this ratio increases there are two corrections to the Maxwell spreading resistance: (i) the Ohmic value is corrected by a factor of the order of unity as pointed by Wexler (1966), and (ii) more important, a dominant ballistic term appears. This was observed by García et al. (2007); Knudsen (1934); Sharvin (1965) and the value of the resistance  $R$  in three dimensions reads (García et al., 2007; Wexler, 1966):

$$R_{3D} = \frac{4\rho(T)\ell}{3A} + \frac{\gamma(\kappa)\rho(T)}{W}, \quad (1)$$

where  $A = \pi W^2/4$  is the area of the hole or constriction and  $\gamma(\kappa)$  is a smooth varying geometrical function, i.e.  $\gamma(\kappa = W/\ell) \simeq 1 - 0.33/\cosh(0.1\kappa) = 0.67 \dots 1$  for  $k = 0 \dots \infty$

(Wexler, 1966). In Eq. (1) the first and the second terms of the right-hand side (rhs) correspond with the Knudsen-Sharvin and Ohmic resistances, respectively. The spreading Ohmic resistance in three dimensions can be estimated within a factor  $2/\pi$  off from the exact Maxwell's solution assuming a hemisphere in which the electric field  $E(r) = J_{3D}(r)\rho(T)$ . The radius  $r$  is taken at the constriction middle point and  $J_{3D}(r)$  is the current density equal to the total current  $I$  divided by half of a sphere, i.e.  $J_{3D}(r) = I/(2\pi r^2)$ , assuming that due to symmetry the current is radial far away from the constriction.

From a similar calculation but in the two dimensional case, appropriate for graphite due to the weak coupling between the graphene planes, we have (García et al., 2008):

$$R_{2D}(T) = a \frac{\rho(T)}{4Wt} \ell(T) + a \frac{2\rho(T)\gamma(\kappa)\ln(\Omega/W)}{\pi t} \Big|_{W < \Omega} + \frac{\rho(T)L}{Wt}. \quad (2)$$

The first term at the right-hand side (rhs) of Eq. (2) corresponds to the ballistic Knudsen-Sharvin resistance; the second, logarithmic term to the ohmic, spreading resistance in two-dimensions; here  $\Omega$  is the total sample width and  $t$  its thickness. The logarithmic dependence on the constriction width of this ohmic, diffusive contribution is due to the quasi-two dimensionality of the transport in graphite and supports the assumption of weakly interacting graphene layers inside the sample. The last term is due to the ohmic resistance of the constriction tube itself. From previous works it was clear that the position and shape of the voltage electrodes affects the outcome of the experiment in mesoscopic devices (McLennan et al., 1991). Therefore the constant  $a$  was introduced, which takes care of the influence of the sample shape, the topology, and the location of the electrodes in the sample. For the usual electrode positions through the whole sample width as shown in Fig. 6,  $a = 1$ . The validity of Eq. (2), especially the logarithmic dependence of the ohmic part, for HOPG as well as for multigraphene samples has been verified by García et al. (2008) and Dusari, Barzola-Quiquia, Esquinazi & García (2011).

In the following, we review some of our experimental results for two multigraphene samples, A and B, with different geometry and resistivity. The sample details as well as their preparation and fabrication were described by Barzola-Quiquia et al. (2008); Dusari, Barzola-Quiquia, Esquinazi & García (2011). The constrictions in the middle of the samples, see Fig. 6, were prepared with the focused-ion beam of a dual-beam microscope. It is important to note that we avoided the modification of the crystalline structure of the samples due to the ion beam spread by protecting them with a  $\sim 300$  nm thick negative-electron beam resist (AR-N 7500), a method successfully tested by Barzola-Quiquia et al. (2010).

To obtain the mean free path without further adjustable parameter we measured the resistance  $R$  as a function of the constriction width  $W$  and use Eq. (2). Figure 7 shows the results for samples A and B at two temperatures. The results show that for  $W < 1 \mu\text{m}$  the ballistic contribution (dashed lines in Figs. 7(a) and (b)) overwhelms the ohmic ones indicating that the mean-free path should be of this order. Having only  $\ell$  as free parameter Eq. (2) can be used to fit the behavior of  $R$  vs.  $W$  for sample A. From the theoretical fits one obtains  $\ell = 1.2 \mu\text{m}$  and  $0.8 \mu\text{m}$  at 60 K and 250 K, respectively. The Fermi wavelength per graphene layer can be calculated using (García et al., 2008):

$$\lambda_F = \frac{1}{a_0} \frac{2\pi\rho(T)\ell(T)e^2}{h}, \quad (3)$$

where  $a_0 = 0.335$  nm is the distance between graphene planes in the graphite Bernal stacking configuration. For sample A we obtain then  $\lambda_F = 0.5(0.8) \pm 0.25 \mu\text{m}$  at 250 K (60 K).

Despite of the good agreement obtained for sample A and for HOPG bulk samples (García et al., 2008), Eq. (2) suffers from an important limitation since it cannot describe correctly ballistic transport phenomenon in which the wave nature of the electrons plays a crucial role, i.e. in samples where  $\lambda_F \gtrsim W$ . As discussed before, in this case the ballistic contribution to the resistance is better described by the quantization of the transverse electron momentum in the constricted region. In this case the value of the resistance is given by the inverse of a sum of an energy-dependent and transverse wave vectors  $q_n$ -dependent transmission probabilities  $T_n$ , where  $n = 0, \pm 1, \pm 2, \dots N_c$  (Stauber et al., 2007). These values correspond to the one dimensional electric sub-bands and  $N_c$  is the largest integer smaller than  $2W/\lambda_F$ . In this case the increase in resistance is expected to show an oscillatory behavior as a function of  $W$  or  $\lambda_F$  (García & Escapa, 1989; Snyman et al., 2008) as observed experimentally in bismuth nanowires (Costa-Krämer et al., 1997) as well as in GaAs devices (van Wees et al., 1988; Wharam et al., 1988).

Note that the obtained mean free path for sample A is smaller than the distance between the electrodes. The larger the sample, larger is the probability to have defective regions with larger carrier concentration and smaller mean free path within the voltage electrodes (Arndt et al., 2009). In order to increase the probability to observe the expected quantization phenomenon in multigraphene samples, it is necessary to have a mean free path larger than the sample size in order to be completely in the ballistic regime. Therefore, we repeated the experiment with sample B that shows lower resistivity and with a smaller voltage-electrode distance, see Fig. 6. Figures 7(c) and (d) show the measured resistance normalized by its value at a constriction  $W = 3 \mu\text{m}$  for sample B. The normalization is necessary because in this way we pay attention to the huge relative increase of  $R$  decreasing  $W$  and we need neither the absolute value of  $\rho$  nor of  $a$  to compare the data with theory. We realize that for sample B Eq. (2) does not describe accurately the experimental data even assuming the largest possible mean-free path equal to the voltage-electrode distance of  $\simeq 2.7 \mu\text{m}$ . The data can be reasonably well fitted dividing the ballistic term in Eq. (2) by the function  $\text{trunc}(2W/\lambda_F)\lambda_F/2W$ , which generates steps whenever the constriction width  $W \simeq i\lambda_F/2$  with  $i$  an integer. From the fits we obtain the parameters  $\lambda_F = 1.0(1.5) \mu\text{m}$  and  $\ell = 2.2(2.7) \pm 0.3 \mu\text{m}$  at 300(10) K. Using other values of  $\ell$ , for example  $\ell = 1.3 \mu\text{m}$ , see Fig. 7(d), the function does not fit the data indicating indeed that the carriers behave ballistically between the voltage electrodes, leaving actually  $\lambda_F$  the only free parameter.

The ballistic analytical function we used resembles the theoretical results with similar steps obtained by Snyman et al. (2008) where the conductance vs.  $W$  was calculated numerically for a single layer graphene with an electrostatically potential landscape that resembles a constriction. An analytical average value or envelope of this stepped function is obtained replacing the truncation function by  $\exp(-\lambda_F/2W)$ , see Figs. 7(c) and (d). This exponential function represents the impossibility of an electron to propagate in the constriction when  $W < \lambda_F/2$ . The important result obtained for sample B is the huge increase of the resistance for  $W < 2 \mu\text{m}$  indicating clearly a larger  $\ell$  than the one obtained in sample A, see Dusari, Barzola-Quiquia, Esquinazi & García (2011) for further details.

The temperature dependence of  $R(T, W)$  can be used now to obtain  $\lambda_F(T)$  and the mobility per graphene layer, this last given by  $\mu(T) = (e/h)\lambda_F(T)\ell(T)$ . Since the density of carriers per graphene layer can be calculated from  $n = 2\pi/\lambda_F^2$  we show in Fig. 8 the mobility vs. carrier density for the two samples and for a bulk HOPG sample and compare them with data from literature for suspended single layer graphene. From these results we clearly recognize the much larger mobility and smaller density of carrier for the graphene layers inside graphite,

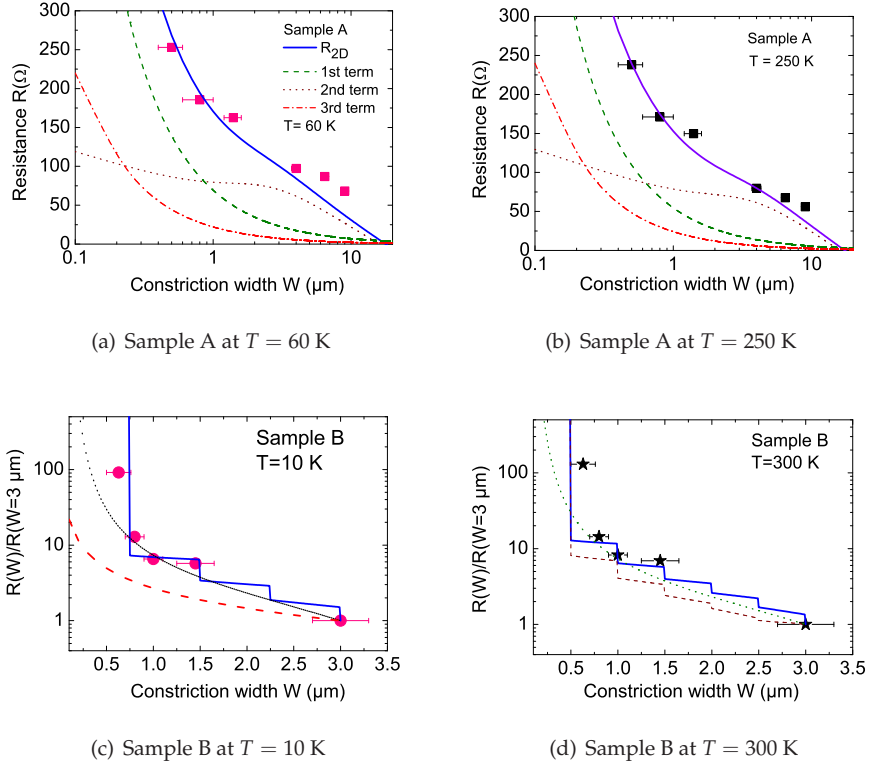


Fig. 7. Measured resistance as a function of the constriction width  $W$  at (a) 60 K and (b) 250 K for sample A. The point with the largest  $W$  corresponds to the virgin sample without a constriction. The different lines correspond to the ballistic contribution (dashed line) and ohmic second (dotted line) and third (dashed-dotted line) terms in Eq. (2). The continuous line represents the addition of the three contributions. For (a) the continuous line is calculated with  $\ell = 1.2 \mu\text{m}$  and for (b)  $\ell = 0.8 \mu\text{m}$ . (c) and (d): Normalized resistance for sample B vs. constriction width  $W$  at 10 and 300 K. Note the semi logarithmic scale. The line with steps is obtained dividing the ballistic term in Eq. (2) by  $(\lambda_F/2W)\text{trunc}(2W/\lambda_F)$  with the parameters  $\ell = 2.7 \mu\text{m}$  and  $\lambda_F = 1.5 \mu\text{m}$ . The dashed line follows Eq. (2). The dotted line is obtained multiplying the ballistic term in Eq. (2) by the exponential function  $\exp(\lambda_F/2W)$ . (d) The same as in (c) but the continuous line was obtained with the parameters  $\lambda_F = 1.0 \mu\text{m}$  and  $\ell = 2.2 \mu\text{m}$ . The dashed stepped function is obtained using the same  $\lambda_F$  but with a smaller  $\ell = 1.3 \mu\text{m}$ . Adapted from Dusari, Barzola-Quiquia, Esquinazi & García (2011).

supporting the view that the graphene layers within graphite are of better quality and with a smaller carrier density than single layer graphene. Obviously neither sample A nor B nor the HOPG sample are free from defects and therefore we expect that the obtained values might still be improved in ideal, defect-free graphite structures.

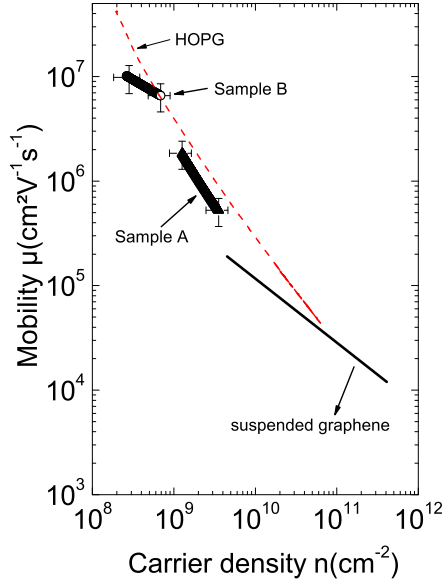


Fig. 8. Mobility vs. carrier density obtained for samples A and B (after Dusari, Barzola-Quiquia, Esquinazi & García (2011)) and for HOPG (dashed line, after García et al. (2008)). Note that the data points are not obtained at a constant temperature but the temperature is changed to get a change in the carrier density and mobility. The points are obtained between 300 K and 10 K for sample B and 300 K and 60 K for sample A. For the HOPG sample (dashed line) the data run from 5 K at the largest mobility values to 300 K. The straight line corresponds to the data of a suspended graphene sample at 20 K from Du et al. (2008).

#### 4. The influence of interfaces inside bulk graphite samples: Hints for the existence of high-temperature superconductivity

##### 4.1 General remarks

Ideal graphite is a layered material where each of the layers (graphene) consists on a honeycomb lattice of carbon atoms. Graphene layers are stacked together with Van der Waals forces much smaller than the covalent ones between the carbon atoms within a single layer. This weak coupling between graphene layers within the graphite structure can be "translated" in a huge anisotropy in the resistivity  $\rho_c/\rho_a \gtrsim 10^6$  at low temperatures. In high quality samples this leads to a quasi-two dimensionality of the transport because most of it occurs within the graphene layers inside the graphite structure (Kopelevich & Esquinazi, 2007). However, real graphite cannot be considered as an ideal uniform stack of ideal graphene layers, as we discussed in Section 2. The role of defects (Arndt et al., 2009; Barzola-Quiquia & Esquinazi, 2010; Barzola-Quiquia et al., 2007) as well as internal interfaces (Barzola-Quiquia et al., 2008) have a crucial effect in the electrical properties. Clear evidence on the non uniformity of real graphite structures is given by several microscopy techniques,



see Section 2. In this Section we are interested in particular on the influence of the internal interfaces on the transport.

#### 4.2 Bulk graphite

Starting with the bulk material, Kempa et al. (2000) studied the magnetoresistance in the in-plane direction in HOPG bulk samples where a magnetic-field-driven transition from metallic- to semiconducting-type behavior of the basal-plane resistance  $\rho_a$  was found. This was reproduced in later publications by other groups (Du et al., 2005; Tokumoto et al., 2004). Note, however, that depending on the thickness of the graphite samples and their quality, metallic or semiconducting behavior in graphite can be observed if no magnetic field is applied (Barzola-Quiquia et al., 2008). There is a clear suppression of the metallic-like phase (in case it appears) by a magnetic field applied perpendicular to the graphene planes (i.e. parallel to the  $c$ -axis) (Kempa et al., 2000). Later work found a field-induced metal-insulator transition (MIT) also in the  $c$ -axis resistivity of graphite  $\rho_c$  (Kempa et al., 2002). The metallic-like behavior of  $\rho_c$  has been related to the one found in the longitudinal resistivity due to a conduction-path mixing mechanism, i.e. the conduction path of the carriers along the  $c$ -axis is in part short circuited by lattice defects and/or impurities.

If non-percolative superconducting grains are located at interfaces running mostly parallel to the graphene planes, the largest increase in the resistance with magnetic field applied parallel to the  $c$ -axis is expected in the temperature region where either the resistance decreases decreasing temperature or it levels off at zero field applied. This is expected since at a temperature below the maximum or leveling off one speculates that the coupling between superconducting grains starts to be observable. Kopelevich et al. (1999) showed a sensitive change in the temperature dependence of the resistivity in bulk HOPG samples under an applied magnetic field parallel to the  $c$ -axis. Additional studies done by Kempa et al. (2003) show the absence of a MIT in graphite if the magnetic field is applied parallel to the graphene planes, a fact that indicates that its origin is related to regions running parallel to the graphene layers.

#### 4.3 Anomalous hysteresis loops and quantum resonances in the magnetoresistance

In percolative homogenous superconducting samples, one can ascribe superconductivity by observing a screening of the external magnetic field (Meissner effect) below a critical field and/or by measuring the drop of resistance to practically zero below a critical temperature. Inhomogeneous granular superconducting materials (in which the superconducting phase could be found in small parts of the whole sample) require other way of testing, as resistance does not drop necessarily to zero and the Meissner effect is probably too small to be measured. Esquinazi et al. (2008) found anomalous hysteresis loops in the MR similar to those observed in granular superconductors with Josephson-coupled grains, see Fig. 9(a).

Esquinazi et al. (2008) and Dusari, Barzola-Quiquia & Esquinazi (2011) show that the minima in the MR are located in the same quadrant field from which one starts the field sweeping as it was reported in conventional high  $T_c$  granular superconductors (Ji et al., 1993). This can be explained based on a two-level critical-state model where pinned fluxons exist inside the Josephson-coupled superconducting grains but also between them. These last ones are usually much less pinned and therefore can strongly influence the MR behavior, especially at low enough fields. The fact that the minimum of the MR is rather flat can be interpreted as due to non-uniform superconducting grain size.

In addition, it must be stressed that when the field is parallel to the graphene planes no effect is observed, suggesting that the superconducting regions or patches are rather parallel to the graphene layers. Quantum resonances in the MR were also observed, see Fig. 9(b), and ascribed to Andreev's reflections between localized superconducting patches connected by semiconducting regions in which Cooper pairs may flow relatively large distances (Esquinazi et al., 2008). From the amplitude and period of the oscillations in field, the distance between superconducting granular domains was estimated to be  $\lesssim 1 \mu\text{m}$  (Esquinazi et al., 2008).

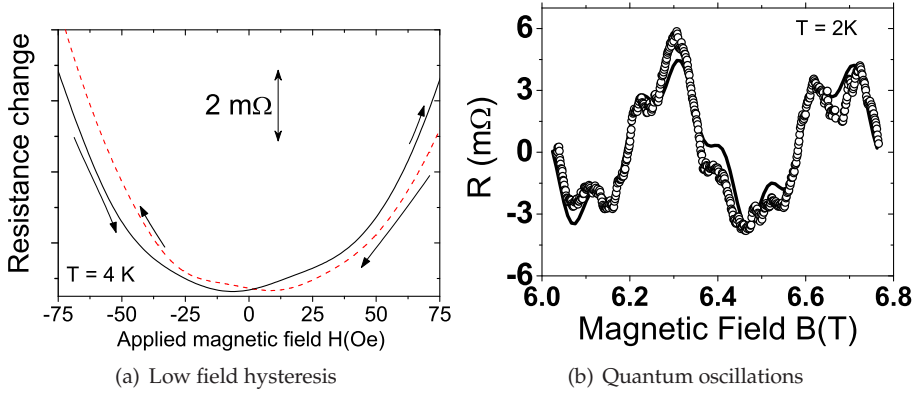


Fig. 9. (a) Weak hysteresis in the resistance of a thin graphite sample vs. magnetic field, similar to that observed in superconductors with Josephson-coupled grains near zero field, measured in a multigraphene sample (after Esquinazi et al. (2008)). (b) Oscillations in the resistance of a multigraphene sample as function of the magnetic field at 2 K after subtraction of a linear field background. The continuous line corresponds to a Fourier fit. Adapted from Esquinazi et al. (2008).

#### 4.4 Behavior of the magnetoresistance of multigraphene samples with micro-constrictions

The novel method of using thin mesoscopic samples with micro-constrictions not only allows us to obtain basic parameters like the mean free path and carrier density, see Section 3, but provides also the possibility to increase the sensitivity of the voltage measurement to the superconducting regions that may be at the constriction region. We mean that the expected superconducting patches inside the constriction area might be better "detected" by usual voltage measurement at two contacts on either side of the constriction. Dusari, Barzola-Quiquia & Esquinazi (2011) verified this effect and found an increase in the range of temperature where the previously reported (Esquinazi et al., 2008) anomalous hysteresis loops can be observed, see Fig. 10.

All the experimental results indicate that, in case that the superconducting regions exist, they should be localized mainly at the interfaces between the crystalline regions of slightly different orientation observed by TEM, see Fig. 2. At these interfaces the density of carriers should be high enough to achieve high critical temperatures, provided the quasi-two dimensionality remains (García & Esquinazi, 2009). The sample can be modeled as the sum of superconducting and normal in series and in parallel circuit paths. A coherent superconducting state at low enough temperatures within the superconducting patches is

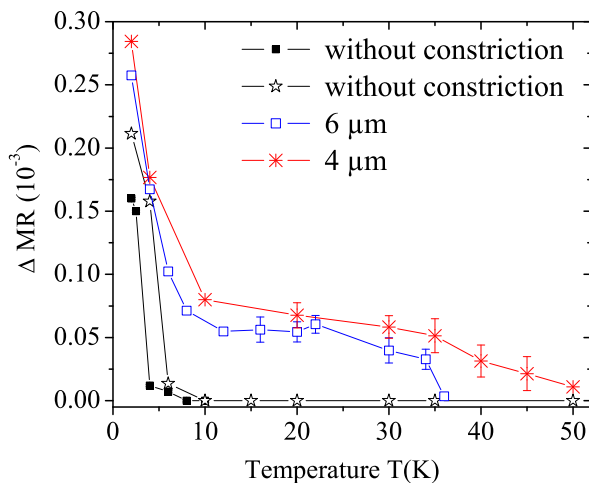


Fig. 10. Relative difference between the two field branches of the hysteresis loop in the MR (see Fig. 9(a)) as a function of temperature for two different multigraphene samples at a constant field of 1.66 mT. Black squares (■) correspond to the data presented by Esquinazi et al. (2008); (\*, □, \*) correspond to the results presented by Dusari, Barzola-Quiquia & Esquinazi (2011) for a multigraphene sample without and with two constrictions. The increase in the hysteresis using the constriction method is clearly seen. The samples without constrictions show granular superconducting-like hysteresis loops up to 10 K only, while samples with the constrictions show this behavior up to 50 K in the case of 4  $\mu\text{m}$  constriction width.

expected as well as in between some of them. Thermal fluctuations influence the coherent superconducting state in some parts of the sample and no zero resistance is achieved. To summarize the results reported so far in tens of nanometers samples as well as the first indications in HOPG bulk samples, two fundamental aspects must be remarked: first, metallic-like behavior of the resistivity in HOPG bulk is not intrinsic and not related to the scattering of conduction electrons with phonons, and second, if superconductivity plays a role in the anomalous properties observed in HOPG samples then the quasi-two dimensional interfaces may contain the superconducting regions (García et al., 2011).

#### 4.5 Transport measurements of TEM lamellae

As explained before, the indications for superconductivity in graphite get clearer when the sample dimensions are reduced to some extent. On the other hand, if the sample dimensions are further reduced, the intrinsic properties of the graphene layers inside graphite can be investigated. In order to further investigate the role of interfaces a different way of preparing samples from bulk graphite seems necessary. The main idea is to prepare small and narrow graphite samples (within the graphene planes) in order to confine the path of the input current to go through some of the possible superconducting interfaces running mostly parallel to the graphene planes. Further details of the process as well as the lamella dimensions can be seen in Fig. 11. Several lamellae have been studied and the results are presented in the following lines.

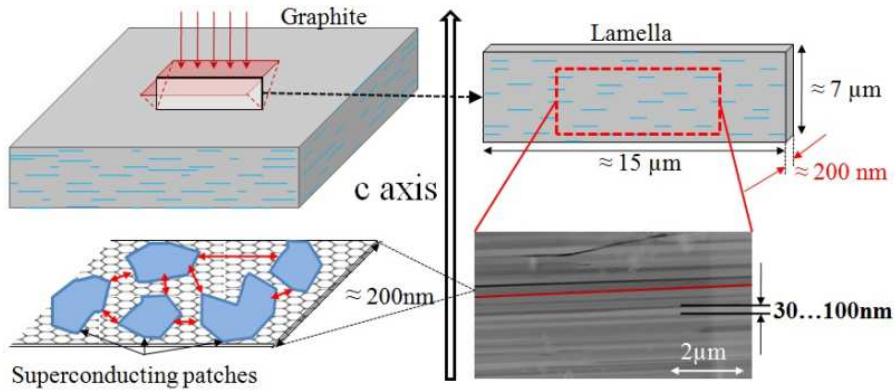


Fig. 11. Sketch of the lamellae preparation process. Focused Ion Beam (FIB) is used to cut bulk HOPG (up left side: reddish areas represent the area to be cut with Gallium ion beam and this last is represented by the red arrows). Previous to this cut, the surface of HOPG is protected with WO thick layer deposited using the electron beam. Lamellae of size  $\sim 7 \mu\text{m} \times 15 \mu\text{m} \times 200 \text{nm}$  (this last dimension in the graphene plane direction) are prepared as shown in the upper right draw. The low-TEM picture (bottom right) shows the interfaces between the crystalline regions (one of them marked in red). Blue lines drawn in the upper pictures provide an idea where the quasi-two dimensional superconducting patches are supposed to be located. The bottom left picture represents how the situation at one of the interfaces might be. The blue areas simulate the superconducting patches that might be weakly, Josephson coupled by low-carrier density graphene regions.

In Fig. 12 we show the change of the voltage vs. temperature measured at two positions in two different lamellae, samples 1 and 2, both prepared using the same procedure. The estimated critical temperatures for these samples are: 25 K and 175 K, respectively, although we should clarify that these temperatures not necessarily are the intrinsic critical temperatures of the patches but probably those related to the Josephson coupling between them. The differences observed in the values of  $T_c$  reflect the inhomogeneous structure expected for the graphite interfaces. Sample 1 results can be considered as the "ideal ones" because within resolution zero values in the voltage are reached for low enough temperatures and small input currents, see Fig. 12(a). In this sample, the used electrical contacts for the voltage measurements were directly at or near some superconducting paths that short circuited below certain temperature and input current. Sample 2 shows similar results, qualitatively speaking, but the range of critical values in temperature and current are different. In this sample the contacts are not placed directly on the superconducting regions and therefore normal regions of the samples contribute to the whole measured voltage. It can be seen in Fig. 12(b) that in this case the transition is sharper and a change of two orders in magnitude in the measured voltage is achieved. Due to the van der Pauw contact configuration used, negative values (respect to the input current direction) of the voltage below the transition temperatures are observed for several lamellae, instead of zero voltage. This can be explained using a Wheatstone bridge circuit as it will be shortly described later in this Section. We found a strong dependence of the measured voltage on the input current. Above a certain current neither negative nor the drop in voltage are observed anymore.

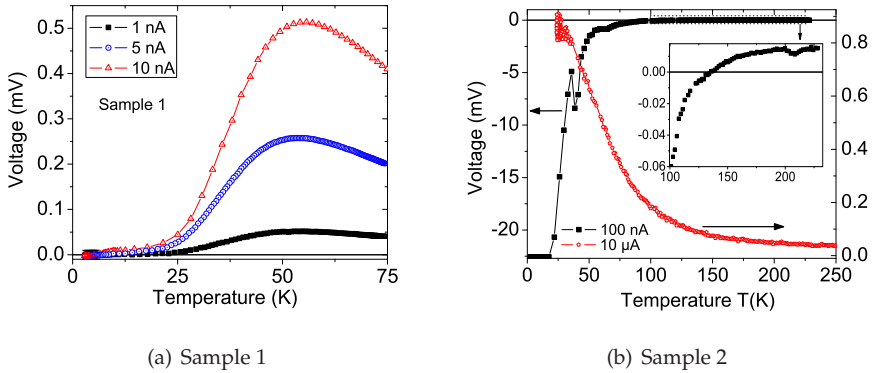


Fig. 12. Voltage vs. temperature measured for two different lamellae. Note the clear change in the temperature dependence with input current. A drop in the measured voltage is observed for all lamellae when the input current is small enough.

Current-Voltage characteristic curves (CVC) are the next important piece of evidence to be mentioned. In case of having Josephson coupling the expected CVC should show a nearly zero voltage value in the measured voltage below a certain value of current and at low enough temperatures. At currents much above a critical one an ohmic linear behavior should be recovered. Another important feature that particularly at low temperature is found in Josephson-coupled systems is the irreversibility in the CVC. As shown in Fig. 13(a) this is achieved in the case of the "ideal" sample 1. The CVC results for other two lamellae become a bit more complex but compatible with the previous results shown in Fig. 12(b). Figures 13(b) and (c) correspond to the CVC for samples 2 and 3, respectively. Negative values in the differential resistance are measured below certain values of current and temperature and above them a linear ohmic behavior is recovered. The simplest way to explain these results is by using a non-homogeneous current-voltage circuit composed by four different resistors  $R_i, i = 1 \dots 4$  within a simple Wheatstone bridge model as for example:  $V(I) \propto I(R_1R_4 - R_2R_3)/((R_1 + R_2)(R_3 + R_4))$ . Each of the  $R_i$  represents an effective resistance within a path inside the lamella. In case one of the resistors includes Josephson-coupled superconducting regions with zero voltage value at low enough temperatures and currents, we can simulate the measured behavior using for this  $R_i$  the CVC given by Ambegaokar & Halperin (1969). Ambegaokar & Halperin (1969) described the voltage vs. current behavior within the DC Josephson effect including thermal noise.

As it can be seen in Figs. 13(b) and (c) the theoretical calculations (solid lines) – using one free parameter (the critical Josephson current) to calculate the corresponding  $R_i(I)$  following Ambegaokar & Halperin (1969) and fixing two or three arbitrary current-independent resistor values for the rest of the Wheatstone circuit – appear to fit well the experimental data. Obviously, pure Josephson-coupled resistors are rather difficult to be observed experimentally because the measured voltage is the sum of contributions coming from the superconducting as well as the semiconducting regions where the first ones are embedded. The case of sample 1 is observed in  $\sim 20\%$  of the measured lamellae.

As shown in Section 4.3 the role of the magnetic field in the granular superconductivity behavior is definitively of huge relevance. When superconducting patches are present

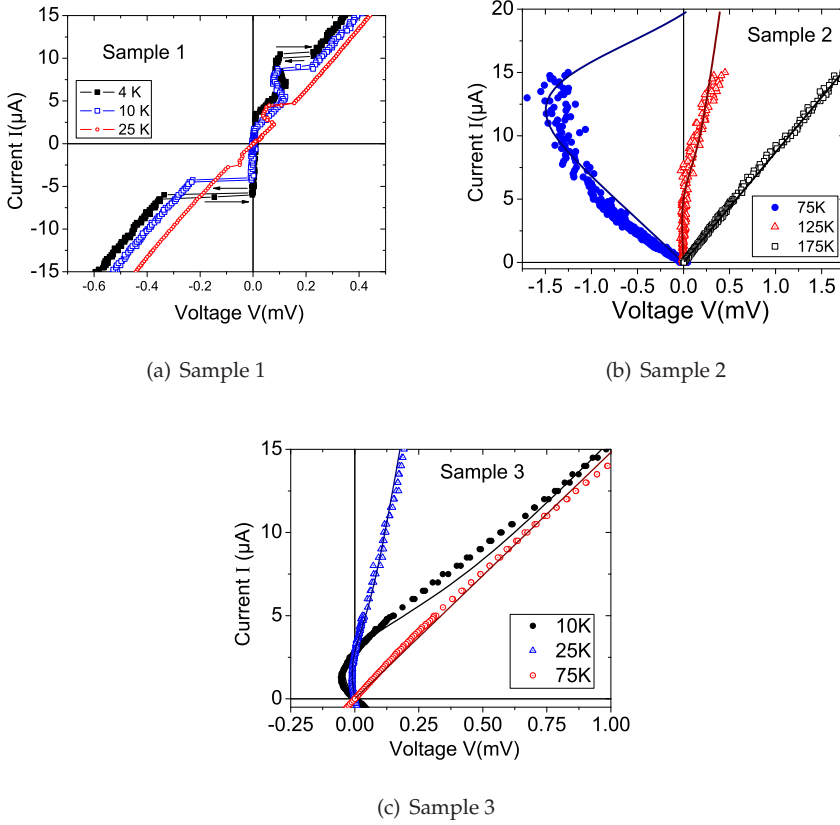


Fig. 13. Current-voltage characteristic curves at different fixed temperatures for three different lamellae. The continuous lines that fit the data were obtained using the Ambegaokar & Halperin (1969) CVC for two  $R_i$ 's in (b) and one  $R_i$  in (c) within a Wheatstone bridge model, assuming different critical Josephson currents at different temperatures. No magnetic field was applied and the earth field was not shielded.

between semiconducting normal regions (we assume that they run mostly parallel to the graphene layers) a remarkable effect must appear when a magnetic field is applied in the  $c$ -axis direction and less influence should be observed if it is applied parallel to the graphene planes. The results in Fig. 14 correspond to the situation where the field is applied parallel to the  $c$ -axis of the lamellae. The in-plane case is not shown here because no effect has been observed, as expected. Figure 14(a) shows the temperature behavior of the measured voltage with and without field. The shift to lower temperatures of the transition after applying 0.75 T is clearly shown for one of the samples. In the case of other sample a 0.1 T field radically changes the previously observed drop in voltage and a semiconducting-like behavior appears. This behavior resembles the MIT found already in HOPG and discussed in Section 4.2. Figure 14(b) shows the CVC at 4 K and 25 K with and without field. One can recognize that the effect of



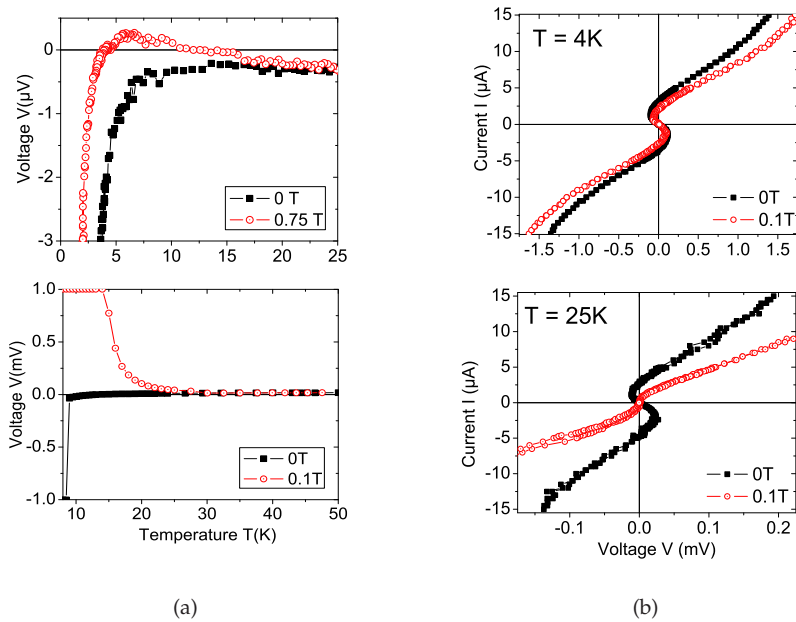


Fig. 14. (a) Voltage dependence on temperature for two different lamellae. Upper picture: The transition denoted by the sharp decrease in the voltage below a certain temperature (black squares) is shifted to lower values when 0.75 T is applied perpendicular to the planes (red dots). Bottom picture: Similar to the other picture but for a different lamella. The zero field (black squares) transition is completely suppressed after applying 0.1 T (red dots). (b) Current-voltage characteristic curves for a different lamella, with (red dots) and without field (black squares) at 4 K (upper graph) and 25 K (bottom graph).

the field is to reduce the superconducting effect, i.e. the CVC tends to a linear, positive voltage behavior.

Heersche et al. (2007) showed that Cooper pairs can flow in a single graphene layer relatively long distances between two superconducting contacts. The authors showed also the existence of Josephson currents. These results support the main idea proposed in this Section concerning the weakly Josephson coupled superconducting regions through a graphene layer. In addition to the work of Heersche et al. (2007), Hagymási et al. (2010) developed a theory for the Josephson critical current in ballistic Superconductor-Graphene-Superconductor structures. We use their model to calculate the reduced temperature dependent critical Josephson current. In Fig. 15 the reader can see the solid line obtained from the model proposed and the experimental data taken from the experimental work described in this Section. The model fits well the data. In the near future further investigations concerning the effect of the magnetic field in these lamellae are needed.

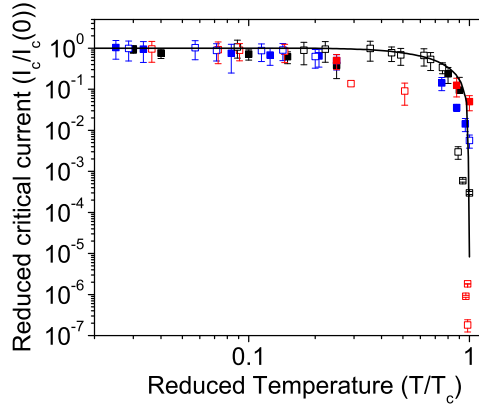


Fig. 15. Normalized Josephson critical current  $I_c/I_c(0)$  as a function of the normalized temperature  $T/T_c$  obtained for different samples. The values obtained for  $I_c(0)$  range from 0.9 to 7  $\mu\text{A}$  and for  $T_c \sim 23$  k to 175 K for different samples. The solid line is the theoretical curve taken from the work of Hagymási et al. (2010) without free parameters.

## 5. Conclusion

The main messages of the work described in this chapter are: (1) Several of the transport properties measured in large graphite samples are not intrinsic of graphite but are influenced in a large extent by interfaces and other defects and impurities. Taking into account that one defect or impurity in a graphene layer inside graphite can contribute with one carrier, it is clear that the carrier densities are not intrinsic but are due to defects and to a large extent probably to highly conducting interfaces, internal as well as at the sample boundaries. We note also that, as the large experimental evidence in semiconductors indicates, even the quantum Hall effect observed in graphite is actually not intrinsic of ideal graphite but can be attributed to the highly conducting quasi-two dimensional electron systems at the interfaces. Clearly, the details of this effect will depend on the sample dimensions and quality, providing us a way to understand experimental discrepancies found in literature. Our work indicates that the intrinsic mobility of the carriers in the graphene layers inside graphite are extraordinarily large  $\mu > 10^6$   $\text{cm}^2/\text{Vs}$  and these carriers show ballistic transport in the micrometer range even at room temperature.

(2) The first observation of superconductivity in doped graphite goes back to 1965 when it was observed in the potassium graphite intercalated compound C8K (Hannay et al., 1965). A considerable amount of studies has reported this phenomenon in intercalated graphite compounds or doped graphite (Emery et al., 2005; Kopelevich et al., 2004; Weller et al., 2005), however the superconducting properties of pure graphite are still under discussion. In this chapter we have given a possible clarification of this topic. By reducing the dimensions of the samples, the intrinsic properties of graphite have been deeper investigated. The overall idea coming out from all the experimental results can be resumed as follows: bulk graphite samples cannot be considered as a uniform electronic system, but it must be considered as a semiconducting matrix with metallic as well as superconducting domains in it. We note that already Lu et al. (2006) realized the coexistence of insulating and

conducting behaviors in bulk graphite surfaces. From this newly acquired knowledge the observed behaviors appear compatible with the existence of non-percolative partially highly conducting, partially superconducting regions coupled by Josephson-coupling through graphene planes. The interfaces observed by TEM may have enough carrier density to trigger quasi-two dimensional superconductivity.

Theoretical work that deals with superconductivity in graphite as well as in graphene has been published in recent years. For example,  $p$ -type superconductivity has been predicted to occur in inhomogeneous regions of the graphite structure (González et al., 2001) or  $d$ -wave high- $T_c$  superconductivity based on resonance valence bonds (Black-Schaffer & Doniach, 2007). Following a BCS approach in two dimensions critical temperatures  $T_c \sim 60$  K have been obtained if the density of conduction electrons per graphene plane increases to  $n \sim 10^{14} \text{ cm}^{-2}$ , a density that might be induced by defects and/or hydrogen ad-atoms (García & Esquinazi, 2009). Further predictions for superconductivity in graphene support the premise that  $n > 10^{13} \text{ cm}^{-2}$  in order to reach  $T_c > 1$  K (Kopnin & Sonin, 2008; Uchoa & Neto, 2007). The interfaces observed by TEM might then be the regions where enough carrier density exists to trigger quasi-two dimensional superconductivity. In contrast to the basically 3D superconductivity in intercalated graphitic compounds (Csányi et al., 2005) we expect that superconductivity at quasi-2D graphite interfaces as well as at doped surfaces (Han et al., 2010) may exist at much higher temperatures, partially because of the role of the high-energy phonons in the 2D graphite structure itself (García & Esquinazi, 2009). Room temperature superconductivity with a  $d + id$  pairing symmetry has been predicted to occur in doped graphene with a carrier concentration  $n \gtrsim 10^{14} \text{ cm}^{-2}$  (Pathak et al., 2010). We note that if we take into account the density of interfaces then a measured carrier density in bulk graphite samples of  $5 \times 10^{12} \text{ cm}^{-2}$  would mean an effective density  $\sim 2 \times 10^{14} \text{ cm}^{-2}$  at the interfaces. And last but not least we refer to a recent theoretical work from Kopnin et al. (2011) where the authors emphasize that a topological protected flat band in semimetals may promote superconductivity at very high temperatures.

## 6. References

- Ambegaokar, V. & Halperin, B. I. (1969). Voltage due to thermal noise in the DC Josephson effect, *Phys. Rev. Lett.* **22**: 1364–1366.
- Arndt, A., Spoddig, D., Esquinazi, P., Barzola-Quiquia, J., Dusari, S. & Butz, T. (2009). Electric carrier concentration in graphite: Dependence of electrical resistivity and magnetoresistance on defect concentration, *Phys. Rev. B* **80**: 195402.
- Barzola-Quiquia, J., Dusari, S., Bridoux, G., Bern, F., Molle, A. & Esquinazi, P. (2010). The influence of  $\text{Ga}^+$  irradiation on the transport properties of mesoscopic conducting thin films, *Nanotechnology* **21**: 145306.
- Barzola-Quiquia, J. & Esquinazi, P. (2010). Ferromagnetic- and superconducting-like behavior of the electrical resistance of an inhomogeneous graphite flake, *J Supercond Nov Magn* **23**: 451–455.
- Barzola-Quiquia, J., Esquinazi, P., Rothermel, M., Spemann, D., Butz, T. & García, N. (2007). Experimental evidence for two-dimensional magnetic order in proton bombarded graphite, *Phys. Rev. B* **76**: 161403(R).
- Barzola-Quiquia, J., Yao, J.-L., Rödiger, P., Schindler, K. & Esquinazi, P. (2008). Sample size effects on the transport properties of mesoscopic graphite samples, *phys. stat. sol. (a)* **205**: 2924–2933.

- Black-Schaffer, A. M. & Doniach, S. (2007). Resonating valence bonds and mean-field  $d$ -wave superconductivity in graphite, *Phys. Rev. B* **75**: 134512.
- Büttiker, M. (1986). Four terminal phase-coherent conductance, *Phys. Rev. Lett.* **57**: 1761.
- Costa-Krämer, J. L., García, N. & Olin, H. (1997). Conductance quantization in bismuth nanowires at 4 K, *Phys. Rev. Lett.* **78**: 4990.
- Csányi, G., Littlewood, P. B., Nevidomskyy, A. H., Pickard, C. J. & Simons, B. D. (2005). The role of the interlayer state in the electronic structure of superconducting graphite intercalated compounds, *Nature Physics* **1**: 42–45.
- Dillon, R. O., Spain, I. L. & McClure, J. W. (1977). Electronic energy band parameters of graphite and their dependence on pressure, temperature and acceptor concentration, *J. Phys. Chem. Solids* **38**: 635–645.
- Drut, J. E. & Lähde, T. A. (2009). Critical exponents of the semimetal-insulator transition in graphene: A Monte Carlo study, *Phys. Rev. B* **79**: 241405(R).
- Du, X., Skachko, I., Barker, A. & Andrei, E. Y. (2008). Approaching ballistic transport in suspended graphene, *Nature Nanotech.* **3**: 491–495.
- Du, X., Tsai, S.-W., Maslov, D. L. & Hebard, A. F. (2005). Metal-insulator-like behavior in semimetallic bismuth and graphite, *Phys. Rev. Lett.* **94**: 166601.
- Dusari, S., Barzola-Quiquia, J. & Esquinazi, P. (2011). Superconducting behavior of interfaces in graphite: Transport measurements of micro-constrictions, *J Supercond Nov Magn* **24**: 401–405.
- Dusari, S., Barzola-Quiquia, J., Esquinazi, P. & García, N. (2011). Ballistic transport at room temperature in micrometer-size graphite flakes, *Phys. Rev. B* **83**: 125402.
- Emery, N., Hérould, C., D’Astuto, M., Garcia, V., Bellin, C., Marêché, J. F., Lagrange, P. & Loupiau, G. (2005). Superconductivity of bulk  $\text{CaC}_6$ , *Phys. Rev. Lett.* **95**: 035413.
- Esquinazi, P., García, N., Barzola-Quiquia, J., Rödiger, P., Schindler, K., Yao, J.-L. & Ziese, M. (2008). Indications for intrinsic superconductivity in highly oriented pyrolytic graphite, *Phys. Rev. B* **78**: 134516.
- García, N., Bai, M., Lu, Y., Chen, H. & Levanyuk, A. P. (2007). Is there ballistic transport in metallic nano-objects? Ballistic versus diffusive contributions, *J. Phys.: Condens. Matter.* **19**: 016212.
- García, N. & Escapa, L. (1989). Elastic oscillatory resistances of small contacts, *Appl. Phys. Lett.* **54**: 1418.
- García, N. & Esquinazi, P. (2009). Mean field superconductivity approach in two dimensions, *J Supercond Nov Magn* **22**: 439–444.
- García, N., Esquinazi, P., Barzola-Quiquia, J. & Dusari, S. (2011). Bernal graphite is a narrow gap semiconductor. arXiv:1106.0437.
- García, N., Esquinazi, P., Barzola-Quiquia, J., Ming, B. & Spoddig, D. (2008). Transition from ohmic to ballistic transport in oriented graphite: Measurements and numerical simulations, *Phys. Rev. B* **78**: 035413.
- González, J., Guinea, F. & Vozmediano, M. A. H. (2001). Electron-electron interactions in graphene sheets, *Phys. Rev. B* **63**: 134421–1–8.
- Grüneis, A., Attacalite, C., Pichler, T., Zabolotnyy, V., Shiozawa, H., Molodtsov, S. L., Inosov, D., Koitzsch, A., Knupfer, M., Schiessling, J., Follath, R., Weber, R., Rudolf, P., Wirtz, R. & Rubio, A. (2008). Electron-electron correlation in graphite: A combined angle-resolved photoemission and first-principles study, *Phys. Rev. Lett.* **100**: 037601.
- Hagymási, I., Kormányos, A. & Cserti, J. (2010). Josephson current in ballistic superconductor-graphene systems, *Phys. Rev. B* **82**(13): 134516.

- Han, S. W., Lee, J. D., Noh, J. P. & Jung, D. W. (2010). Superconductivity of a calcium-doped graphite  $\text{CaC}_{30}$ , *J. Low Temp. Phys.* **160**: 41–48.
- Hannay, N. B., Geballe, T. H., Matthias, B. T., Andres, K., Schmidt, P. & MacNair, D. (1965). Superconductivity in graphitic compounds, *Phys. Rev. Lett.* **14**: 7.
- Heersche, H. B., Jarillo-Herrero, P., Oostinga, J. B., Vandersypen, L. M. K. & Morpurgo, A. F. (2007). Bipolar supercurrent in graphene, *Nature* **446**: 56–59.
- Herrmann, R., Kraak, W., Nachtwei, G. & Worm, G. (1984). Shubnikov-de Haas effect of n-inversion layers in InSb grain boundaries, *Solid State Commun.* **52**: 843–845.
- Ji, L., Rzchowski, M. S., Anand, N. & Thinkam, M. (1993). Magnetic-field-dependent surface resistance and two-level critical-state model for granular superconductors, *Phys. Rev. B* **47**: 470–483.
- Kelly, B. T. (1981). *Physics of Graphite*, London: Applied Science Publishers.
- Kempa, H., Esquinazi, P. & Kopelevich, Y. (2002). Field-induced metal-insulator transition in the *c*-axis resistivity of graphite, *Phys. Rev. B* **65**: 241101(R).
- Kempa, H., Esquinazi, P. & Kopelevich, Y. (2006). Integer quantum Hall effect in graphite, *Solid State Communication* **138**: 118–122.
- Kempa, H., Kopelevich, Y., Mrowka, F., Setzer, A., Torres, J. H. S., Höhne, R. & Esquinazi, P. (2000). Magnetic field driven superconductor-insulator-type transition in graphite, *Solid State Commun.* **115**: 539–542.
- Kempa, H., Semmelhack, H. C., Esquinazi, P. & Kopelevich, Y. (2003). Absence of metal-insulator transition and coherent interlayer transport in oriented graphite in parallel magnetic fields, *Solid State Commun.* **125**: 1–5.
- Knudsen, M. (1934). *Kinetic theory of gases*, London: Methuen.
- Kopelevich, Y., da Silva, R. R., Torres, J. H. S., Moehlecke, S. & Maple, M. B. (2004). High-temperature local superconductivity and graphite-sulfur composites, *Physica C* **408**: 77–78.
- Kopelevich, Y. & Esquinazi, P. (2007). Graphene physics in graphite, *Adv. Mater. (Weinheim, Ger.)* **19**: 4559.
- Kopelevich, Y., Lemanov, V., Moehlecke, S. & Torres, J. (1999). Landau level quantization and possible superconducting instabilities in highly oriented pyrolytic graphite, *Phys. Solid State* **41**: 1959–1962.
- Kopelevich, Y., Torres, J. H. S., da Silva, R. R., Mrowka, F., Kempa, H. & Esquinazi, P. (2003). Reentrant metallic behavior of graphite in the quantum limit, *Phys. Rev. Lett.* **90**: 156402–1–4.
- Kopnin, N. B., Heikkilä, T. T. & Volovik, G. E. (2011). High-temperature surface superconductivity in topological flat-band systems. arXiv: 1103.2033.
- Kopnin, N. B. & Sonin, E. B. (2008). *Phys. Rev. Lett.* **100**: 246808.
- Kumar, A., Poumirol, J.-M., Escoffier, W., Goiran, ., Raquet, B. & Pivin, J. C. (2010). High magnetic field induced charge density waves and sign reversal of the Hall coefficient in graphite, *J. Phys.: Condens. Matter* **22**: 436004.
- Landauer, R. (1957). Spatial variation of currents and fields due to localized scatterers in metallic conduction, *IBM J. Res. Dev.* **1**: 223.
- Lu, Y., Muñoz, M., Steplecaru, C. S., Hao, C., Bai, M., García, N., Schindler, K. & Esquinazi, P. (2006). Electrostatic force microscopy on oriented graphite surfaces: Coexistence of insulating and conducting behaviors, *Phys. Rev. Lett.* **97**: 076805. See also the comment by S. Sadewasser and Th. Glatzel, *Phys. Rev. Lett.* **98**, 269701 (2007) and the reply by

- Lu et al., *idem* **98**, 269702 (2007) and also R. Proksch, *Appl. Phys. Lett.* **89**, 113121 (2006).
- Ludwig, F., Nachtwei, G., Watts, M., Bassom, N. J., Müller, H.-U., Kraak, W., Gille, P. & Nicholas, R. J. (1992). Cyclotron resonance of the quasi-two-dimensional electron gas at  $\text{Hg}_{1-x}\text{Cd}_x\text{Te}$  grain boundaries, *Semicond. Sci. Technol.* **7**: 511–515.
- McClure, J. W. (1964). Energy band structure of graphite, *IBM J. Res. Dev.* **8**: 255.
- McLennan, M. J., Lee, A. & Datta, S. (1991). Voltage drop in mesoscopic systems: A numerical study using a quantum kinetic equation, *Phys. Rev. B.* **43**: 13846.
- Pathak, S., Shenoy, V. B. & Baskaran, G. (2010). Possible high-temperature superconducting state with a  $d + id$  pairing symmetry in doped graphene, *Phys. Rev. B* **81**: 085431.
- Schneider, J. M., Orlita, M., Potemski, M. & Maude, D. K. (2009). Consistent interpretation of the low-temperature magnetotransport in graphite using the Slonczewski-Weiss-McClure 3d band-structure calculations, *Phys. Rev. Lett.* **102**: 166403.
- Sharvin, Y. V. (1965). A possible method for studying Fermi surfaces, *Sov. Phys. JETP.* **21**: 655.
- Snyman, I., Tworzydło, J. & Beenakker, C. W. J. (2008). Calculation of the conductance of a graphene sheet using the Chalker-Coddington network model, *Phys. Rev. B* **78**: 045118.
- Stauber, T., Peres, N. M. R. & Guinea, F. (2007). Electronic transport in graphene: A semiclassical approach including midgap states, *Phys. Rev. B* **76**: 205423.
- Tokumoto, T., Jobiliong, E., Choi, E., Oshima, Y. & Brooks, J. (2004). Electric and thermoelectric transport probes of metal-insulator and two-band magnetotransport behavior in graphite, *Solid State Commun.* **129**: 599.
- Tsidilkovski, I. M. (1997). *Electron Spectrum of Gapless Semiconductors*, Vol. 116 of *Springer Series in Solid-State Sciences*, Springer Verlag.
- Tsu, R. & Esaki, L. (1973). Tunneling in a finite superlattice, *Appl. Phys. Lett.* **22**: 562.
- Uchida, S., Landwehr, G. & Bangert, E. (1983). Electric subbands in p-type germanium inversion layers, *Solid State Commun.* **45**: 869–872.
- Uchoa, B. & Neto, A. H. C. (2007). Superconducting states of pure and doped graphene, *Phys. Rev. Lett.* **98**: 146801.
- van Wees, B. J., van Houten, H., Beenakker, C. W. J., Williamson, J. G., Kouwenhoven, L. P., van der Marel, D. & Foxon, C. T. (1988). Quantized conductance of point contacts in a two-dimensional electron gas, *Phys. Rev. Lett.* **60**: 848.
- Vul, B. M. & Zavaritzkaya, E. Y. (1979). Two dimensional electronic phenomena in bicrystals of germanium at He temperatures, *Zh. Eksp. Teor. Fiz.* **76**: 1089–1099.
- Weller, T. E., Ellerby, M., Siddharth, S. S., Smith, R. P. & Skippe, T. (2005). Superconductivity in the intercalated graphite compounds  $\text{C}_6\text{Yb}$  and  $\text{C}_6\text{Ca}$ , *Nature Phys.* **1**: 39–41.
- Wexler, G. (1966). The size effect and the non-local boltzmann transport equation in orifice and disk geometry, *Proc. Phys. Soc. London* **89**: 927.
- Wharam, D. A., Thornton, T. J., Newbury, R., Pepper, M., Ahmed, H., Frost, J. E. F., Hasko, D. G., Peacockt, D. C., Ritchie, D. A. & Jones, G. A. C. (1988). One-dimensional transport and the quantisation of the ballistic resistance, *J. Phys. C: Solid State Phys.* **21**: L209.
- Zhang, Y., Small, J. P., Pontius, W. V. & Kim, P. (2005). Fabrication and electric-field-dependent transport measurements of mesoscopic graphite devices, *Appl. Phys. Lett.* **86**: 073104.